

A biopsy tool with integrated piezoceramic elements for needle tract cauterization and cauterization monitoring

Karthik Visvanathan · Tao Li · Yogesh B. Gianchandani

Published online: 6 September 2011
© Springer Science+Business Media, LLC 2011

Abstract This paper reports the feasibility of biopsy needle tract cauterization and cauterization monitoring using an embedded array of piezoceramic microheaters. Circular heaters of lead zirconate titanate (PZT-5A), with 200 μm diameter and 70–80 μm thickness, are fabricated using a batch mode micro ultrasonic machining process. These are then assembled into cavities in the walls of 20-gauge stainless steel needles and sealed with epoxy. Experiments are performed by inserting the proposed biopsy needle into porcine tissue samples. The needle surface exceeds the minimum target temperature rise of 33°C for either radial or thickness mode vibrations. The corresponding input power levels are 236 mW and 325 mW, respectively. The tissue cauterization extends 1–1.25 mm beyond the perimeter of the needle and is uniform in all directions. After cauterization, the fundamental anti-resonance frequency and the corresponding impedance magnitude of the PZT heater decrease by 4.1% and 42.6%, respectively, thereby providing a method to monitor the extent of tissue cauterization. A sensing interface circuit capable of measuring the resonance frequency shift of the PZT elements is built and tested using discrete integrated circuit components. The circuit detects the resonance frequency shift from 8.22 MHz to 7.96 MHz of the PZT elements when the biopsy needle is inserted into wax medium. An interface circuit for actuation of the PZT elements for tissue cauterization is also described.

Keywords Ultrasound · Ablation · Microheater

1 Introduction

Needle aspiration biopsy is a diagnostic procedure used to investigate the presence of tumor cells (Amedee and Dhurandhar 2001). A major surgical (or open) biopsy can be avoided by instead performing the needle aspiration biopsy. The needle aspiration biopsy is less traumatic than an open surgical biopsy, making it widely accepted as a diagnostic method for detection of thyroid, liver, kidney, lungs, bones and pancreas cancers.

Even though percutaneous biopsies are safe, there have been reports of potential risks of complications such as deposition of tumor cells or “seeding” along the needle tract. This can lead to the spread of tumor cells to new regions (Takamori et al. 2000; Ryder 2003). The percentage of seeding rates has ranged from 0.6% to 12.5% for fine needle aspiration (FNA) biopsies for hepatocellular carcinoma (Pelloni and Gertsch 2000; Llovet et al. 2001). Seeding rates for biopsies using the cutting needle technique has varied from 0.76% to 3.4% (Durand et al. 2001; Kim et al. 2000; Huang et al. 1996). Subcutaneous tumor seeding after FNA biopsies of metastatic colonic adenocarcinoma (Goletti et al. 1992) and metastatic pancreatic adenocarcinoma (de Sio et al. 2002) has also been reported.

Another probable complication that occurs with percutaneous needle biopsies is hemorrhage. Studies suggest that post biopsy hematoma in the liver can be as high as 18.3% and 23% with 2 mm Tru-cut needles and 1.6 mm Jamshidi needles, respectively (Sugano et al. 1991; Minuk et al. 1987). Further, this percentage can be higher for patients with cirrhosis and uncorrected coagulopathy (Piccinino et

K. Visvanathan (✉) · Y. B. Gianchandani
Department of Mechanical Engineering, University of Michigan,
Ann Arbor, MI, USA
e-mail: vkarthik@umich.edu

T. Li · Y. B. Gianchandani
Department of Electrical Engineering and Computer Science,
University of Michigan,
Ann Arbor, MI, USA

al. 1986). Another study suggests that minor to severe bleeding occurs in 90% of the patients after percutaneous needle biopsies (Ralls et al. 1987). Various techniques have been used in the past for promoting blood clotting after percutaneous needle biopsies. These approaches involve trans-needle placement of steel coils (Allison and Adam 1988) and injection of fibrin (Chisholm et al. 1989), gelatin particles and thrombin (Zins et al. 1992), gelatin sponge pledgets (Smith et al. 1996; Fandrich et al. 1996), and fibrinogen and thrombin (Falstrom et al. 1999; Paulson et al. 2000). These techniques do not provide a solution to the possibility of tumor cell deposition along the needle tract (Pritchard et al. 2004). Biopsy needle tract cauterization is a therapeutic option that can simultaneously avoid post biopsy hemorrhage and needle tract seeding (Fig. 1). Cauterization promotes blood clotting as well as kills tumor cells deposited along the needle tract.

Numerous tissue cauterization methods have been used in the past. The most common method used for tissue cauterization is RF ablation (Haase and Noguera 1962; Schuster and Wolf 2001). In this technique, AC current at radio frequencies flowing through a biological tissue results in heat generation. The use of laser energy for tissue cauterization has been investigated by Mizutani et al (1992). Microwaves have also been used for thermal ablation of biological tissue (Durville et al. 1999). Ultrasound energy in the form of high intensity focused ultrasound (HIFU) has been used for tissue cauterization for hemostasis and hyperthermia. Ultrasound transducers made of cylindrical elements for omni-directional heating have also been reported (Hynynen 1992; Jarosz 1996; Diederich et al. 1999). Planar (Chopra et al. 2000) and weakly focused (Lafon et al. 2002) elements with rotation have been reported for selective heating of targeted tissue.

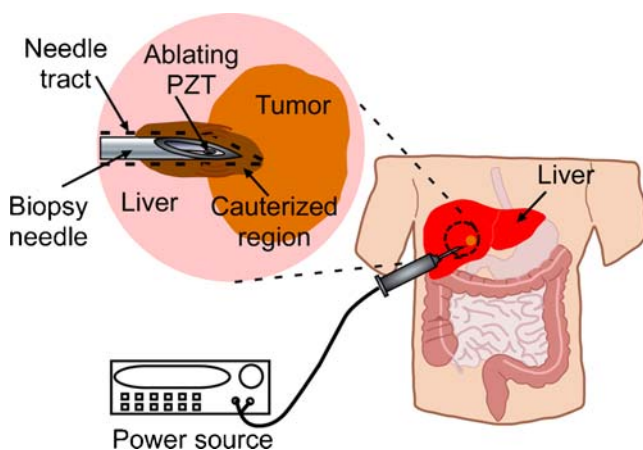


Fig. 1 Concept diagram of an ultrasonic cauterization device for needle tract cauterization during biopsy procedure

Makin et al. (2005) has described an approach for tissue ablation using a 32 element array of PZT elements with a total size of $2.3 \times 49 \text{ mm}^2$.

Past work on biopsy needle tract cauterization has been limited to RF ablation. Animal studies of RF ablation using the biopsy needle itself have been discussed by Kim et al (1993). Comparison of hemorrhage after liver and kidney biopsies with and without the needle tract cauterization has been studied by Pritchard et al. (2004). The use of RF ablation by the introducer needle reduces bleeding in liver and kidney by 63% and 97%, respectively.

Other cauterization methods have not been explored for this application probably due to the manufacturing challenges associated with the integration of these methods with the biopsy needles. The batch mode micro ultrasonic machining process (μ USM) (Li and Gianchandani 2006) allows the microfabrication of lead zirconate titanate (PZT) elements with good piezoelectric properties that can be easily assembled into the sidewall of a needle. The advantage of using PZT elements is the ability to monitor the change in the tissue properties based on the change in electromechanical impedance characteristics of the PZT elements around the resonance frequency. This can provide a method to monitor the extent of tissue cauterization, thereby limiting the extent of damage sustained by the surrounding healthy tissue. For instance, Li et al. have reported a micromachined piezoelectric sensor integrated into a cavity in a biopsy needle for real time tissue differentiation (Li et al. 2007).

A simple and inexpensive interface circuit for the measurement of the resonance frequency shift due to tissue cauterization also warrants attention. The circuits typically used for measurement of resonance frequency shift, which include impulse excitation circuits, phase locked loops and oscillator circuits, have been focused on quartz crystal microbalances (Eichelbaum et al. 1999). These techniques either require a computer or microprocessor or a high quality factor for the sensor. However, the PZT elements have a lower quality factor as compared to quartz elements. In addition, in this application the resonance is highly damped by the surrounding media for heat generation. A hill climbing algorithm capable of locking onto the frequency of maximum vibration amplitude of cantilever structures has been reported (Fan et al. 2011); it used photo-detectors for measuring the vibration amplitude, which are not amenable to use with biopsy tools. In this paper we describe a purely electronic adaptation that is capable of locking onto the local minima in the impedance curve around the resonance frequency of the PZT element. In addition, an interface circuit that can be easily integrated with the proposed resonance frequency measurement circuit for actuation of the PZT heaters is also described.

The paper¹ is organized in the following manner. Section 2 describes the system design. Section 3 describes the simulation models used in this work. Section 4 describes the fabrication of the proposed biopsy tool and the interface circuits used in the experiments. Section 5 describes the experimental results. Section 6 presents the conclusions.

2 System design

The initial portion of this section describes the design of the proposed biopsy tool. The latter portion of Section 2 describes the design of the interface circuit for sensing of tissue cauterization.

2.1 Biopsy tool design

The schematic of the proposed biopsy tool design is shown in Fig. 2. A recess located in the wall of a biopsy needle houses the PZT discs. The PZT discs are inset into the wall to maintain the patency of the lumen. The outer wall of the needle remains smooth, and therefore does not change the penetration characteristics. The PZT discs are placed in this recess to prevent it from blocking the path for acquiring tissue during the biopsy procedure. The thin nature of the diaphragm formed by the outer wall beneath the recess reduces the heat loss due to conduction through the needle. The PZT discs are surrounded by epoxy to provide a highly damping medium for heat generation as well as reduce the heat loss due to conduction. The biopsy needle serves as the ground plane for the PZT discs. A thin copper wire within the lumen provides electrical connection to the top electrode.

2.2 Interface circuit design

Figure 3(a) shows the block diagram of the proposed interface circuit for measurement of the resonance frequency shift of the PZT element. It consists of a voltage controlled oscillator (VCO), a low pass filter, a current to voltage converter, a peak detection circuit and an adder circuit.

Figure 3(b) shows the typical electromechanical impedance spectrum of a PZT element around the resonance frequency. Assume that an initial voltage, V_{in} , is used to generate a square wave signal from the VCO at frequency f_1 (Fig. 3(b)). The low-pass filter converts the square wave signal into a sine

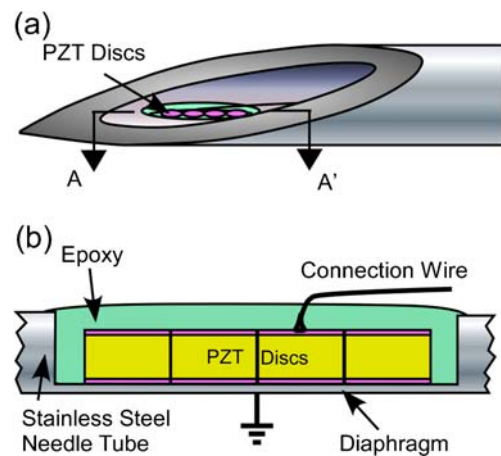


Fig. 2 (a) Schematic diagram of the proposed biopsy tool. (b) Schematic of the cross-section view of the proposed biopsy tool

wave signal and is then applied to the PZT element. The current to voltage converter generates a voltage signal proportional to the current flowing through the PZT element; the peak is provided as a feedback signal to the VCO through an adder. This increases the output signal frequency of the VCO from f_1 to f_2 (Fig. 3(b)). Since the impedance of the PZT element at f_2 is lower than that at f_1 , the amplitude of the AC

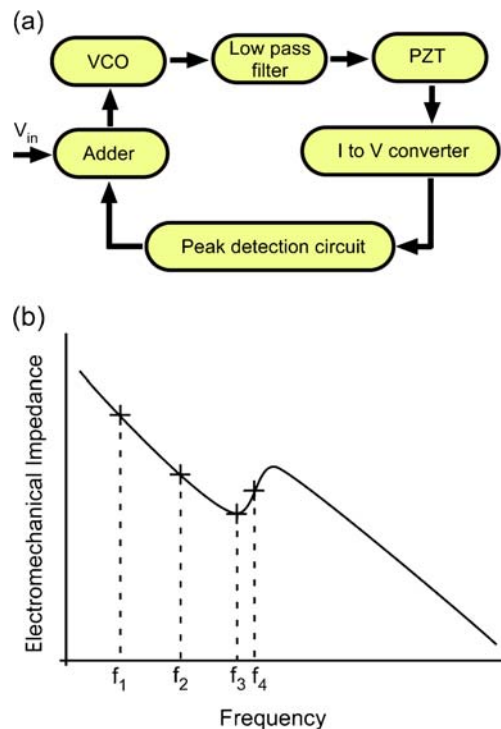


Fig. 3 (a) The block diagram of the proposed readout circuit for measurement of the resonance frequency shift of the PZT heaters due to tissue cauterization. (b) Schematic of a typical electromechanical impedance curve of a PZT element around its resonance frequency

¹ Portions of this paper have been published in conference abstract form in (Visvanathan et al. 2010a, b)

current flowing through the PZT element increases. This, in turn, increases the voltage output from the peak detection circuit, which further increases the frequency of the output signal from the VCO. This process is repeated until the frequency of the output signal of the VCO approaches f_3 . The change in the signal frequency from f_3 to f_4 leads to an increase in the impedance of the PZT element, which, in turn, reduces the feedback voltage. Thus, the output frequency of the system settles around f_3 , which is the resonance frequency of the PZT element.

3 Simulation model

The initial portion of this section describes the simulation model for estimating the temperature profile generated by the PZT heater and the analytical model for calculating the resonance frequency shift of the PZT element due to tissue cauterization. The latter portion of Section 3 describes the simulation model for estimating the performance of the proposed interface circuit.

3.1 Tissue ablation model

A 3D finite element model was used to estimate the temperature profile generated by the PZT heaters in the biological tissue surrounding the biopsy needle. Pennes' bioheat transfer model is used to model the heat transfer in tissue (Pennes 1948). The model uses the following equation:

$$\rho_t c_t \frac{\partial T}{\partial t} = \nabla \cdot k \nabla T + \rho_b c_b \omega_b (T_b - T) + \dot{q} \quad (1)$$

where ρ_t is the density, c_t is the specific heat capacity, k is the thermal conductivity, T is the temperature, ρ_b is the density of blood, c_b is the specific heat capacity of blood, ω_b is the perfusion rate of the blood, T_b is the arterial blood temperature and \dot{q} is the heat generation rate per unit volume due to an ultrasound applicator. The perfusion rate accounts for the cooling due to blood flow in the surrounding fluid.

For the structure used in this work, PZT elements are significantly smaller than the size of the needle. Hence it is permissible to model the elements as small spherical sources. The heat generation rate in the surrounding medium due to the damping of ultrasound waves is given by (Skinner et al. 1998):

$$\dot{q} = \frac{2\alpha I_s r_0^2}{r^2} e^{-2\alpha(r-r_0)} \quad (2)$$

where α is the ultrasound absorption coefficient, I_s is the ultrasound intensity along the surface of the transducer, r is the radial distance from the center of the transducer and r_0 is the radius of the transducer. Due to inefficiencies in the

transducer, not all the electrical energy provided to it is converted into acoustic energy. This unconverted energy is dissipated, within the transducer as heat. For a given transducer efficiency, ν , the heat generation rate per unit volume within the transducer is estimated by:

$$\dot{q}_{app} = \left(\frac{1-\nu}{\nu} \right) \frac{3I_s}{r_0} \quad (3)$$

The simulations were performed using the bioheat equation model in COMSOL Multiphysics®. Three designs were considered in the simulations: a single PZT disc, a PZT array (4 discs) with no gap between elements, and a PZT array with 0.5 mm gaps between elements (Fig. 4(a)). Each of these models included four major regions: PZT heater, epoxy surrounding the PZT heater, biopsy needle and biological tissue. The biological tissue was modeled by a 5 cm diameter sphere surrounding the needle. The 20

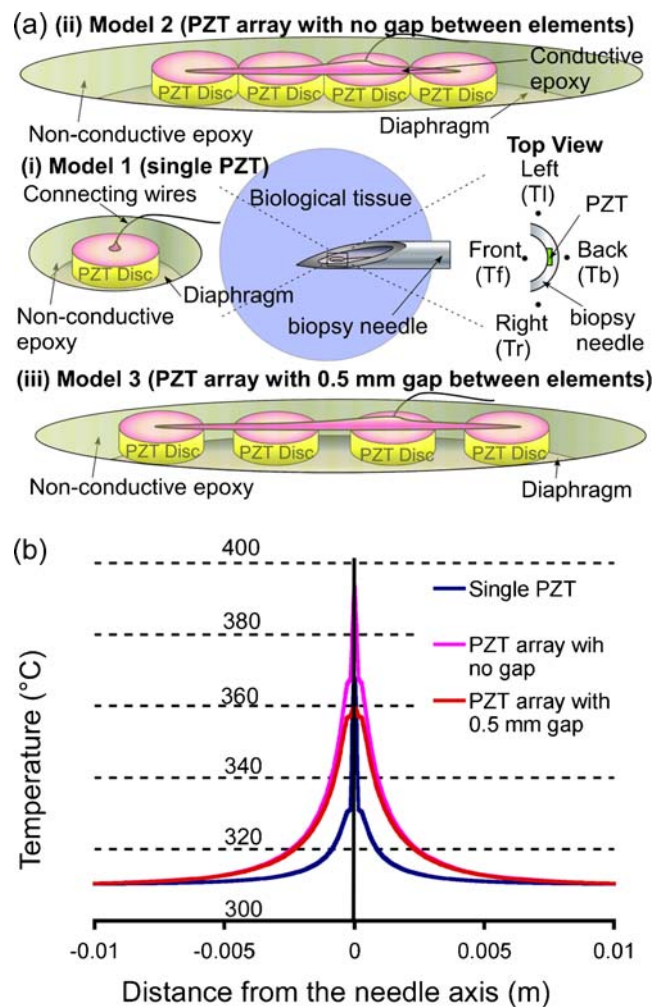


Fig. 4 (a) Schematic model of various biopsy tool designs considered in the simulation. (b) Finite element simulation results for the variation of temperature as a function of distance from the needle for the three designs for ultrasound intensity, $I_s=90 \text{ W.cm}^{-2}$

gauge needle used in the experiments was modeled by a semi-circular cylinder with inner and outer radii of 300 μm and 450 μm , respectively. The length of the needle was 6 cm. For the single PZT element design, a hole of 135 μm depth and 300 μm diameter modeled the cavity in which the PZT heater was located. For the arrayed element design, a slot of $2,000 \times 300 \times 135 \mu\text{m}^3$ was used. The material properties used in the simulations are listed in Table 1.

The cooling due to blood flow was considered only in the biological tissue region. The heat generation rate given by Eq. 2 was used in the epoxy, needle and tissue region. The heat generation rate given by Eq. 3 was used in the PZT region. The outer surface of the tissue was assumed to be at 310 K. The base of the needle extending outside the tissue region was assumed to be at 300 K. For a PZT transducer operating at a frequency of 7 MHz with an input power density level of 50 W.cm^{-2} , the transducer efficiency, as identified in the context of Eq. 3, was determined to be 0.52 (Tyreus & Diederich 2002). In the present simulations, with transducer frequency of 10 MHz and input power density level of 90 W.cm^{-2} , the transducer efficiency was assumed to be 0.52.

Figure 4(b) compares the simulation results for the variation of temperature as a function of distance from the needle. Simulations suggest that for an ultrasound surface intensity of 90 W.cm^{-2} , maximum temperature rise is attained by the PZT array with no gap between the elements. The ultrasound surface intensity is directly proportional to the drive voltage applied to the electrodes of the PZT elements. Hence, in the experiments, biopsy needles with an embedded array of four PZT discs with no gap between the elements were used.

Table 1 Material properties used in the simulations

Density of tissue	$1,050 \text{ kg.m}^{-3}$
Thermal conductivity of tissue	$0.51 \text{ W.m}^{-1}.\text{K}^{-1}$
Specific heat capacity of tissue	$3,639 \text{ J.kg}^{-1}.\text{K}^{-1}$
Density of blood	$1,000 \text{ kg.m}^{-3}$
Specific heat capacity of blood	$4,180 \text{ J.kg}^{-1}.\text{K}^{-1}$
Perfusion rate of blood	$15 \times 10^{-3} \text{ s}^{-1}$
Arterial blood temperature	310 K
Thermal conductivity of needle	$44.5 \text{ W.m}^{-1}.\text{K}^{-1}$
Density of needle	$7,850 \text{ kg.m}^{-3}$
Specific heat capacity of needle	$475 \text{ J.kg}^{-1}.\text{K}^{-1}$
Thermal conductivity of epoxy	$1.7 \text{ W.m}^{-1}.\text{K}^{-1}$
Density of epoxy	$1,060 \text{ kg.m}^{-3}$
Specific heat capacity of epoxy	$1,000 \text{ J.kg}^{-1}.\text{K}^{-1}$
Thermal conductivity of PZT	$1 \text{ W.m}^{-1}.\text{K}^{-1}$
Density of PZT	$7,700 \text{ kg.m}^{-3}$
Specific heat capacity of PZT	$350 \text{ J.kg}^{-1}.\text{K}^{-1}$

3.2 Model for estimating resonance frequency shift due to cauterization

A modified Butterworth-Van-Dyke circuit model can be used to determine the variation in impedance characteristics of the PZT element around the resonance frequency—in air, and in tissue, before and after cauterization (Pan et al. 2006; Bandey et al. 1999). The resonance frequency and the magnitude of the electromechanical impedance of a PZT-embedded structure at the resonance frequency depend on the density, elastic modulus and loss factor of the surrounding medium. The elastic modulus and loss factor of the tissue increase due to ablation, thereby providing a method for monitoring tissue cauterization (Kiss et al. 2004).

Figure 5(a) shows the schematic of the modified Butterworth-Van-Dyke circuit. The circuit model consists of a static branch (C_0). The static branch describes the fixed dielectric capacitance of the PZT element. In parallel with this branch are an infinite number of motional branches (R_n, L_n, C_n), each corresponding to different resonance

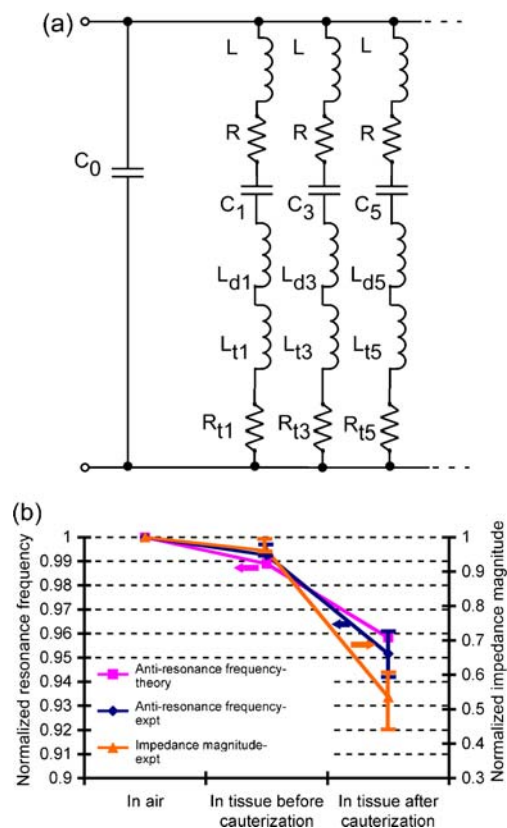


Fig. 5 (a) Modified Butterworth Van Dyke (BVD) equivalent circuit for predicting the shift in resonance frequency due to tissue cauterization. (b) Analytical modeling results and experimental results for the variation of anti-resonance frequency and impedance magnitude at resonance when the biopsy needle tip is in air, and in tissue before and after cauterization

modes. The motional branches determine the resonance characteristics such as the resonance frequency and quality factor of various resonance modes. The various resistors, capacitors and inductors in the circuit are given by (Li et al. 2007; Pan et al. 2006):

$$C_0 = \frac{\varepsilon A}{t_0} \quad (4)$$

$$L = \frac{1}{4\pi^2 f_{r1}^2 c_1} \quad (5)$$

$$C_n = \frac{8k_t^2/n^2\pi^2}{1 - 8k_t^2/n^2\pi^2} C_0 \quad (6)$$

$$R = \frac{\eta_0}{\rho_0 \nu_0^2 c_1} \left(\frac{f}{f_{a1}} \right) \quad (7)$$

where k_t is the electro-mechanical coupling constant, η_0 is the viscosity of PZT layer, ρ_0 is the density of PZT, A is the area of PZT element, ν_0 is the acoustic velocity in PZT, t_0 is the PZT element thickness and ε is the dielectric permittivity in PZT. The fundamental resonance, f_{r1} , (minimum impedance) and anti-resonance (maximum impedance) frequency, f_{a1} , are given by:

$$f_{r1} = \frac{1}{2\pi\sqrt{LC_1}} \quad (8)$$

$$f_{a1} = \sqrt{1 + \frac{C_1}{C_0}} f_{r1} \quad (9)$$

The effect of the needle diaphragm loading is modeled by adding an inductor L_{dn} to the motional branch of the circuit. The inductor L_{dn} is given by (Li et al. 2007):

$$L_{dn} = \frac{4f_{a1}L\rho_m t_m}{n\rho_0\nu_0} \quad (10)$$

where ρ_m and t_m are the density and the thickness of the needle diaphragm, respectively. The effect of tissue loading is modeled by adding a resistor R_m and inductor L_m to the motional branch of the circuit. For a semi-infinite viscoelastic medium R_m and L_m are given by (Bandey et al. 1999):

$$R_m = \frac{n\pi}{4k_t^2\omega C_0 Z_q} \left[\frac{\rho_t(|G| + G')}{2} \right]^{0.5} \quad (11)$$

$$L_m = \frac{n\pi}{4k_t^2\omega^2 C_0 Z_q} \left[\frac{\rho_t(|G| - G')}{2} \right]^{0.5} \quad (12)$$

$$Z_q = \sqrt{E_0\rho_0} \quad (13)$$

$$G = G' + i\eta\omega \quad (14)$$

where E_0 is the elastic modulus of PZT, ρ_t is the tissue density, ω is the operation frequency, G' is the tissue storage modulus, η is the loss factor in tissue and Z_q is the PZT acoustic impedance.

Table 2 lists the material properties used in the model. Because the fundamental radial resonance mode of the PZT element is used in the experiments, the variation of the anti-resonance frequency of this mode is calculated. The variation of the anti-resonance frequency when the biopsy needle tip is in air, in tissue before cauterization, and in tissue after cauterization is shown in Fig. 5(b). Analytical modeling results suggest that the fundamental anti-resonance frequency decreases by 3.1% after cauterization. Experimental results are also plotted in Fig. 5(b) which will be discussed in Section 4.

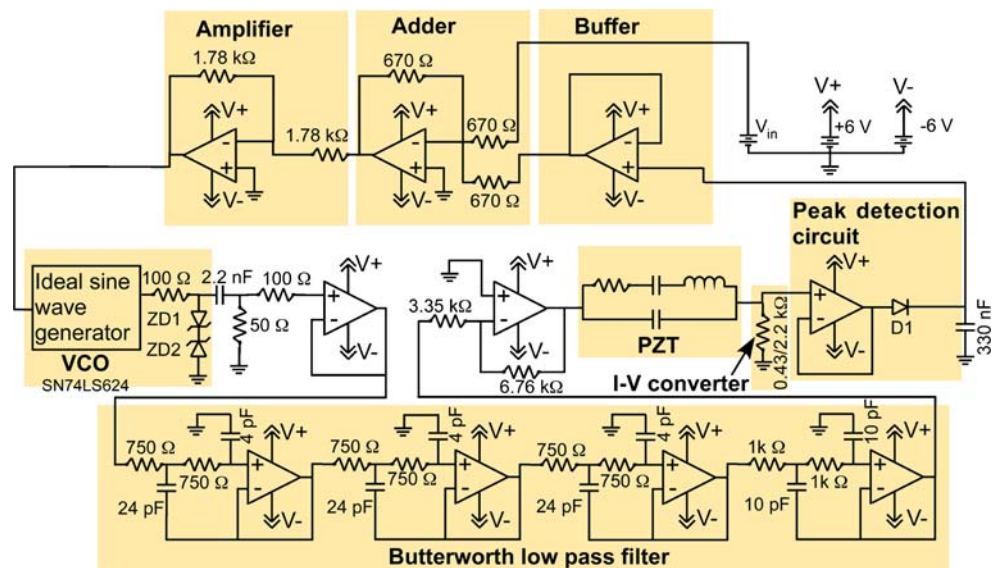
3.3 Interface circuit for sensing of tissue cauterization

The performance of the proposed interface circuit for measurement of the resonance frequency shift of the PZT elements was verified using simulations in PSpice®. Figure 6 shows the schematic of the circuit used in the simulations. The voltage-controlled square-wave oscillator was modeled using an ideal sine wave generator connected to two Zener diodes (Fig. 6). The PZT element was

Table 2 Material properties used in the BVD analytical model

Normal tissue	
Density, ρ_t	1,054 kg.m ⁻³
Storage modulus, G'	550 Pa
Loss factor, η	13 Pa.s
Cauterized tissue	
Storage modulus, G'	37,000 Pa
Loss factor, η	230 Pa.s
PZT-5A	
Young's modulus, E_0	5.2×10^{10} Pa
Density, ρ_0	7,800 kg.m ⁻³
Coupling constant, K_t	0.72
Relative dielectric constant	1,800
Needle diaphragm	
Density	8,030 kg.m ⁻³
Thickness	40 μ m

Fig. 6 Schematic of the sensing circuit for detection of the resonance frequency shift of the PZT element due to tissue cauterization



modeled using the Butterworth Van Dyke circuit as shown in Fig. 6. In this model, only the fundamental resonance mode was considered. Hence only one motional branch was used in the simulations. The resonance frequency is given by Eq. 8. The resonance frequency of the PZT element can be varied by changing either the value of motional inductor, or motional capacitor. A 430 Ω resistor connected in series with the PZT element was used as the current to voltage converter.

Transient simulations were performed in PSpice to verify the functioning of the proposed circuit. The output of the circuit for various resonance frequencies was tested by varying the value of the motional capacitor in the BVD model. Simulations were also performed for equivalent models of both weakly and strongly damped PZT elements by varying the value of the motional resistor (R_1). Motional resistor values of 500 Ω and 3,500 Ω were used to model the weakly and strongly damped PZT elements, respectively. In these simulations, the static capacitor and the motional inductor values were assumed to be 18.91 pF and 463.6 μH. The simulation results are shown in Fig. 7. The circuit worked

well for equivalent models of weakly damped PZT elements in the frequency range of 7 MHz to 11.5 MHz, and strongly damped PZT elements in the range of 7.5 MHz to 10 MHz.

4 Fabrication

4.1 Biopsy tool

The PZT discs were fabricated from PZT-5A material as it has a Curie temperature of 350°C, which is greater than the target temperature of 70–100°C ($\Delta T=33\text{--}63^\circ\text{C}$). Circular PZT elements were used because for a given volume of the device, these generate higher temperature rise per unit voltage as compared to square and rectangular devices (Visvanathan et al. 2009). The PZT discs (of diameter 200 μm and thickness 70–80 μm) were fabricated using batch mode micro μUSM (Li and Gianchandani 2006) (Fig. 8a). The μUSM tools were fabricated using micro electro-discharge machining (μEDM) of a stainless steel substrate. Figure 9a shows the SEM image of a fabricated μUSM tool. The patterns were then transferred to the PZT-5A plate using μUSM with tungsten carbide slurry (Fig. 9b). Tungsten carbide powders of 0.5–0.99 μm diameter were used in these machining steps (Alldyne Powder Technologies, Huntsville, Al). The patterned PZT discs were released by lapping the substrate from behind. A 50 nm thick titanium layer and a 500 nm thick gold layer were sputtered onto the PZT discs to form the electrodes. The sides of the discs were covered with a thin layer of photoresist to prevent shorting of the two electrodes during sputtering.

The PZT discs were integrated into a recess ($2,000 \times 300 \times 135 \mu\text{m}^3$) cut into 20-gauge stainless steel needles (Becton Dickinson, Franklin lakes, NJ, Model #:305175)

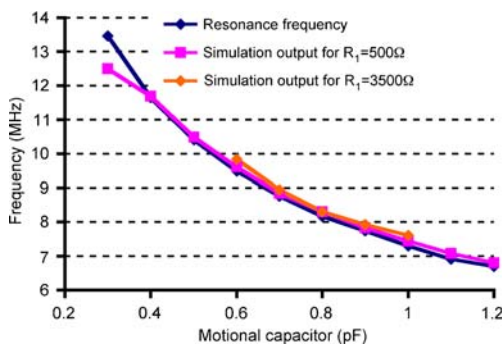


Fig. 7 PSpice simulation results of the circuit for low ($R_1=500 \Omega$) and highly damped ($R_1=3,500 \Omega$) PZT elements

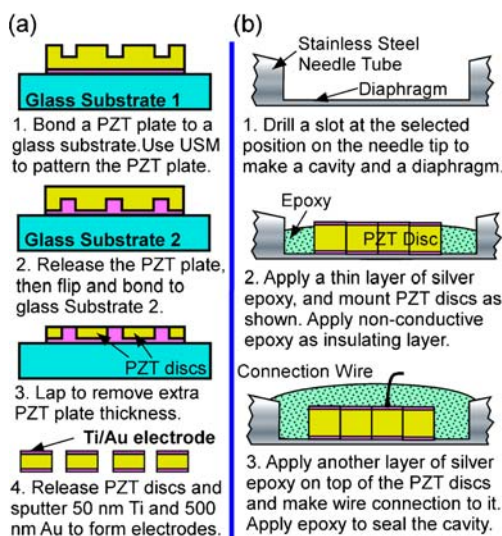


Fig. 8 (a) The μ USM process for PZT disc fabrication. (b) PZT disc integration procedure for the biopsy tool

using μ EDM (Fig. 8(b)). The discs were bonded to the biopsy needle using conductive epoxy. Figure 9c shows the photograph of a biopsy needle with four discs integrated into the recess. The discs were surrounded by non-conductive epoxy to electrically isolate the top and bottom electrodes. A flexible copper wire bonded using a layer of conductive epoxy, within the lumen provided power to the top electrode while the needle provided the ground return path.

4.2 Interface circuit

The sensing circuit was built and tested using discrete integrated chip (IC) components on a printed circuit board (PCB) (Advanced Circuits Inc., Aurora, CO) and breadboards. A four layer PCB design was used. The intermediate layers consisted of a ground plane and a split power plane to supply power to the op-amps. A separate power line of 5 V was used to supply power to the VCO. A SN74LS624 IC (Texas Instruments Inc., Dallas, TX) was used as the VCO. The VCO was capable of generating signals with frequencies up to 20 MHz which was greater than the targeted range of 7–12 MHz. The voltage feedback amplifiers, AD8056, (Analog Devices Inc., Norwood, MA) were used for AC signal processing. Op-amps LM741 (National Semiconductor Inc., Santa Clara, CA) were used for DC signal processing.

The actuation interface circuit for the PZT heater consists of a MOSFET driver (MD1213, Supertex Inc.) and high voltage *p* and *n* channel FETs (TC6320) (Visvanathan et al. 2011). This circuit can provide signals with peak to peak amplitudes up to ± 100 V and frequencies up to 20 MHz. In addition, it also has a source and sink current capability of ± 2 A.

5 Experimental results

The initial portion of this section presents the experimental results on feasibility of tissue cauterization and the cauterization monitoring using the proposed biopsy tool. The latter portion discusses the experimental results obtained from the interface circuits.

5.1 Tissue cauterization

The temperature profile generated by the biopsy tool was measured for both resonance modes: the radial mode (10.3 MHz) and the thickness mode (22.3 MHz). The PZT discs had a low quality factor because of the high damping provided by the surrounding epoxy. Hence, there was only a single combined peak observed in the electromechanical impedance curve despite the use of four discs. For this experiment, the actuation was performed by a sinusoidal waveform generated through a function generator and a power amplifier. The temperature was measured using a K-type thermocouple which is read by a digital thermometer. The experiments were performed by inserting the needle into porcine tissue samples. Figure 10a shows the temperature measured at different distances and directions from a needle for the radial mode. The temperature distribution was similar in all directions for both resonance modes. This indicated uniform cauterization in the surrounding region.

The temperature rise at the surface of the needle, in both resonance modes, for varying input voltage was also measured. The needle surface exceeded the minimum target temperature rise of 33°C for an applied voltage of $17 V_{\text{RMS}}$ and $14 V_{\text{RMS}}$ for radial and thickness mode, respectively. This difference is believed to be mainly due to the higher

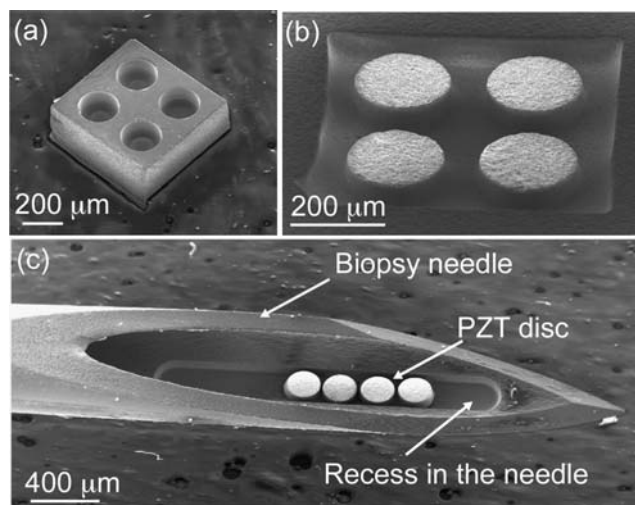


Fig. 9 (a) SEM image of the tool used in the μ USM process. (b) SEM image of the pattern transferred onto a PZT substrate using the μ USM process. (c) SEM image of the PZT discs assembled into a recess made on the wall of a biopsy needle using μ EDM

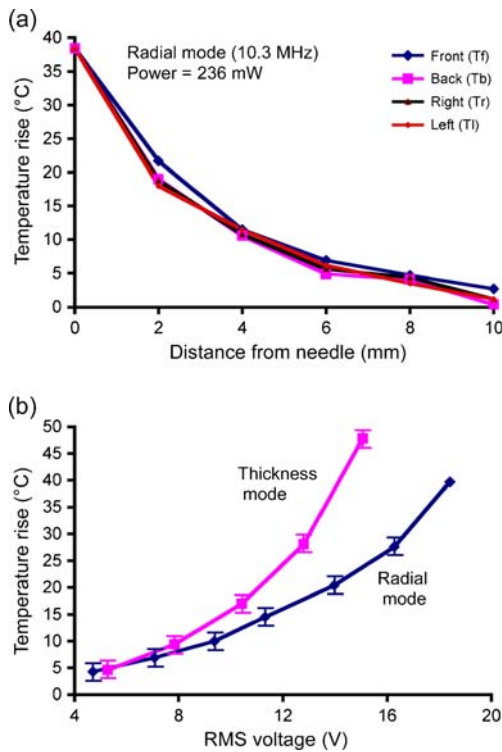


Fig. 10 (a) Variation of temperature as a function of direction and distance from the needle for the radial mode for an input power of 236 mW. The temperature distribution is similar in all directions. (b) Variation in the temperature generated at the surface of the needle for various input power

electromechanical impedance of the PZT device at lower operating frequency. Figure 10(b) compares the temperature rise generated at the surface of the needle for various input power for the two modes. The experiments suggested that the target temperature rise of 33°C was achieved for input power of 236 mW and 325 mW, respectively. Figure 11 shows the photographs of the cauterized porcine tissue. The visible radius of tissue cauterization was 1–1.25 mm beyond the perimeter of needle.

5.2 Sensing of the tissue cauterization

Porcine tissue samples were cauterized by actuating the PZT discs with an RMS voltage of 14 V at the fundamental

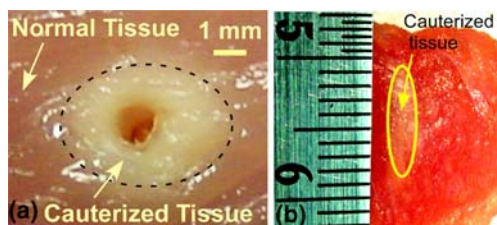


Fig. 11 Photograph of (a) top view and (b) cross section of the cauterized porcine tissue. The radius of cauterization beyond the perimeter of the needle was 1–1.25 mm for an input RMS voltage of 14 V

anti-resonance frequency of 9.6 MHz. Figure 4(b) shows the variation of the impedance characteristics of the PZT transducer (measured at room temperature, using an impedance analyzer—Agilent 4395A) for the following three cases: biopsy needle tip in air, in tissue before and after cauterization. The fundamental anti-resonance frequency (f_{a1}) of the PZT discs was used for monitoring of cauterization. The f_{a1} and the impedance magnitude values at resonance were normalized to the value obtained when the needle was in air. After cauterization, f_{a1} and the impedance magnitude decreased further by 4.1% and 42.6%, respectively (Fig. 4(b)). This decrease matches to that predicted by the analytical model and can be used to monitor the progress of cauterization. The variation in f_{a1} was also measured with temperature varied in the range for cauterization while the needle tip stayed in air. Even though f_{a1} decreased (from 11.92 MHz to 11.38 MHz) with increasing temperature (from 22°C to 78°C), it was observed that f_{a1} returned to its initial value when the needle was cooled down to room temperature (Fig. 12). As the readings in Fig. 4(b) were all made at the same room temperature, additional correction is not necessary.

5.3 Interface circuit

Experiments were performed using the biopsy tool operated with the portable circuit to determine the resonance frequency of the PZT heaters (Visvanathan et al. 2011). The resonance frequency of the PZT heater integrated biopsy tool in air, and embedded in wax medium, as measured by an impedance analyzer, were 8.22 MHz and 7.96 MHz, respectively. The corresponding resonance frequencies measured using the circuit were 8.2–8.27 MHz and 7.96–8 MHz, respectively. The experiments indicate that the circuit was able to successfully detect the resonance frequency shift of 0.26 MHz. For actuation amplitudes up to 13 V, the actuation circuit worked in the desired frequency range of 5–12 MHz.

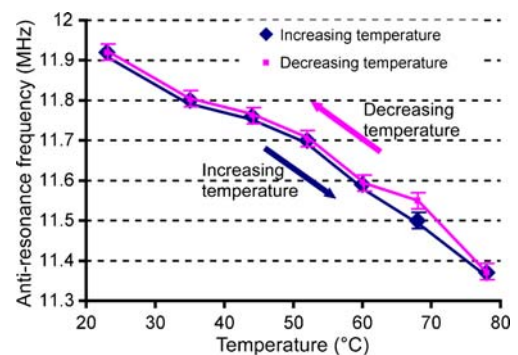


Fig. 12 Measured variation of anti-resonance frequency (f_{a1}) with temperature in the range used for cauterization. The f_{a1} returned to the original value in the range of temperatures from body temperature to room temperature

6 Conclusions

This work showed the feasibility of biopsy needle tract cauterization and cauterization monitoring using PZT heaters embedded into the wall of biopsy needles. Finite element simulations suggested that a PZT array with no gap between the elements was most suitable for generating maximum temperature rise for a given driving voltage. An analytical model based on modified Butterworth-Van-Dyke circuit model suggested that the resonance frequency of the PZT element decreased when the tissue was cauterized. The PZT heaters generated the target temperature rise of 33°C for an input power of <325 mW and a drive voltage of <17 V_{RMS}. The extent of tissue cauterization was <1.25 mm beyond the perimeter of the needle thereby ensuring minimum damage to the surrounding tissue. This is desired as for this application it is only necessary to cauterize the tissue layer in contact with the needle. Cauterization of porcine tissue sample resulted in a decrease of 4.1% in the resonance frequency and 42.6% in the peak impedance magnitude, thereby providing a method to monitor the extent of cauterization. The interface circuit for measurement of resonance frequency shift of the PZT heater during cauterization were also described. The circuit was built and tested on a PCB using discrete IC components. The circuit was able to track the resonance frequency shift from 8.22 MHz to 7.96 MHz when the needle was inserted into wax medium. An interface circuit for actuation of the PZT heaters was also discussed. The circuit generated the desired signal in the frequency range of 5–10 MHz. This approach bears significant promise in the long term for developing miniaturized servo-controlled cauterization procedure. Additional experiments involving live tissue samples and post cauterization tissue analysis studies will be addressed in future efforts.

Acknowledgement Portions of study related to piezothermal heat generation were supported in part by Defense Advanced Research Projects Agency Microsystems Technology office (DARPA-MTO). KV acknowledges partial support by a fellowship from the Mechanical Engineering department at University of Michigan.

References

- D.J. Allison, A. Adam, *Radiology* **169**, 261–263 (1988)
- R.G. Amedee, N.R. Dhurandhar, *Laryngoscope* **111**, 1551–1557 (2001)
- H.L. Bandey, S.J. Martin, R.W. Cernosek, *Anal. Chem.* **71**, 2205–2214 (1999)
- R.A. Chisholm, S.N. Jones, W.R. Lees, *Clin. Radiol.* **40**, 627–628 (1989)
- R. Chopra, M.J. Bronskill, F.S. Foster, *Medical Physics* **27**, 1281–1286 (2000)
- I. de Sio, L. Castellano, M. Calandra, C. Del Vecchio-Blanco, *European Journal of Ultrasound* **15**, 65–68 (2002)
- C.F. Diederich, W.H. Nau, P.R. Stauffer, *IEEE Trans. Ultrason. Ferroelectr. Freq. Control.* **46**, 1218–1228 (1999)
- F. Durand, J.M. Regimbeau, J. Belghiti, A. Sauvanet, V. Vilgrain, B. Terris, V. Moutardier, O. Farges, D. Valla, *J. Hepatol.* **35**, 254–288 (2001)
- F.M. Durville, R.R. Rediker, R.J. Connolly, S.D. Schwaitzberg, J. Lantis, *SPIE Conference on Gastrointestinal Surgery*, San Jose, 1999, 420–424
- F. Eichelbaum, R. Borngraber, J. Shroder, R. Lucklum, *Review of Scientific Instruments* **70**, 2537–2545 (1999)
- J.K. Falstrom, M.M. Moore, S.H. Caldwell, A.H. Matsumoto, R.D. Abbott, W.D. Spotnitz, *J. Vasc. Interv. Radiol.* **10**, 457–462 (1999)
- X.Z. Fan, N. Siwak, R. Ghodssi, *Journal of Micromechanics and Microengineering* **21**, 045008 (2011)
- C.A. Fandrich, R.P. Davies, P.M. Hall, *Australas. Radiol.* **40**, 230–234 (1996)
- O. Goletti, M. Chiarugi, P. Bucciati, P. Macchiarini, *Eur. J. Surg. Oncol.* **18**, 636–637 (1992)
- F.R. Haase, J.T. Noguera, *Arch. Otolaryngol.* **75**, 125–126 (1962)
- G.T. Huang, J.C. Sheu, P.M. Yang, H.S. Lee, T.H. Wang, D.S. Chen, *J. Hepatol.* **25**, 334–338 (1996)
- K. Hynynen, *Medical Physics* **19**, 979–987 (1992)
- B.J. Jarosz, *IEEE Trans. Biomed. Eng.* **43**, 1106–1115 (1996)
- E.H. Kim, K.K. Kopecky, O.W. Cummings, R.G. Dreesen, D.C. Pound, *Investig. Radiol.* **28**, 228–230 (1993)
- S.H. Kim, H.K. Lim, W.J. Lee, J.M. Cho, H.J. Jang, *Abdominal Imaging* **25**, 246–250 (2000)
- M.Z. Kiss, T. Varghese, T.J. Hall, *Physics in Medicine and Biology* **49**, 4207–4218 (2004)
- C. Lafon, D.M. de Lima, Y. Theilli re, F. Prat, J.Y. Chapelon, D. Cathignol, *Medical Physics* **29**, 290–297 (2002)
- T. Li, Y.B. Gianchandani, *Journal of Microelectromechanical Systems* **15**, 605–612 (2006)
- T. Li, R.Y. Gianchandani, Y.B. Gianchandani, *Lab on a Chip* **7**, 179–185 (2007)
- J.M. Llovet, R. Vilana, C. Bru, L. Bianchi, J.M. Salmeron, L. Boix, S. Ganau, M. Sala, M. Pages, C. Ayuso, M. Sole, J. Rodes, J. Bruix, Barcelona clinic liver cancer group, *Hepatology* **33**, 1124–1129 (2001)
- I.R.S. Makin, T.D. Mast, W. Faidi, M.R. Runk, P.G. Barthe, M.H. Slayton, *Ultrasound in Medicine and Biology* **31**, 1539–1550 (2005)
- G.Y. Minuk, L.R. Sutherland, D.A. Wiseman, F.R. MacDonald, D.L. Ding, *Gastroenterology* **92**, 290–293 (1987)
- T. Mizutani, H. Takanari, H. Suzuki, K. Wada, T. Mizumoto, T. Sato, S. Namikawa, M. Kusagawa, *Journal of Clinical Laser Medicine and Surgery* **10**, 223–228 (1992)
- W. Pan, P. Soussan, B. Nauwelaers, H.A.C. Tilmans, *Sensors and Actuators A* **126**, 436–446 (2006)
- E.K. Paulson, G.R. Stephenson, M.C. Neal, V. Rossin, J.H. Lawson, *J. Vasc. Interv. Radiol.* **11**, 905–911 (2000)
- A. Pelloni, P. Gertsch, *Schweiz Med Wochenschr* **130**, 871–877 (2000)
- H.H. Pennes, *J. Appl. Physiol.* **1**, 93–122 (1948)
- F. Piccinino, E. Sagnelli, G. Pasquale, G. Giusti, *J. Hepatol.* **2**, 165–173 (1986)
- W.F. Pritchard, D.W. Cahen, J.W. Karanian, S. Hilbertand, B.J. Wood, *J. Vasc. Interv. Radiol.* **15**, 183–187 (2004)
- P.W. Ralls, J.A. Barakos, E.M. Kaptein, P.E. Friedman, G. Fouladian, W.D. Bose, J. Halls, S.G. Massry, *J. Comput. Assist. Tomogr.* **11**, 1031–1034 (1987)
- S.D. Ryder, *Gut* **52**, 1–8 (2003)
- T.G. Schuster, J.S. Wolf, *J. Urol.* **165**, 1968–1970 (2001)
- M.G. Skinner, M.N. Iiuzuka, M.C. Kolios, M.D. Sherar, *Physics in Medicine and Biology* **43**, 3535–3547 (1998)
- T.P. Smith, V.G. McDermott, D.M. Ayoub, P.V. Suhocki, D.J. Stackhouse, *Radiology* **198**, 769–774 (1996)
- S. Sugano, Y. Sumino, T. Hatori, H. Mizugami, T. Kawafune, T. Abei, *Dig. Dis. Sci.* **36**, 1229–1233 (1991)
- R. Takamori, L.L. Wong, C. Dang, L. Wong, *Liver Transplantation* **6**, 67–72 (2000)

- P.D. Tyreus, C.J. Diederich, *Physics in Medicine and Biology* **47**, 490–498 (2002)
- K. Visvanathan, Y.B. Gianchandani, *IEEE International Conference on Solid-State Sensors, Actuators, and Microsystems (Transducers)*, Denver, Colorado, 2009, 2421–2424.
- K. Visvanathan, Y.B. Gianchandani, *IEEE/ASME International Conference on Micro Electro Mechanical Systems (MEMS 10)*, Hong Kong, 2010, 987–1000.
- K. Visvanathan, T. Li, Y.B. Gianchandani, *International Conference on Miniaturized Systems for Chemistry and Life Sciences (MicroTAS 2010)*, Groningen, The Netherlands, 2010, 1478–1480.
- K. Visvanathan, *Ph.D. Thesis, University of Michigan*, 2011
- M. Zins, V. Vilgrain, S. Gayno, Y. Rolland, L. Arrive, M.H. Denninger, M.P. Vullierme, D. Najmark, Y. Menu, H. Nahum, *Radiology* **184**, 841–843 (1992)